

# Quasi-static Incremental Behavior of Granular Materials: Elastic–Plastic Coupling and Micro-scale Dissipation

Matthew R. Kuhn<sup>a,\*</sup>, Ali Daouadji<sup>b</sup>

<sup>a</sup>*Br. Godfrey Vassallo Prof. of Engrg., Donald P. Shiley School of Engrg., Univ. of Portland, 5000 N. Willamette Blvd., Portland, OR, USA 97231*

<sup>b</sup>*University of Lyon, INSA-Lyon, GEOMAS, F-69621, France*

---

## Abstract

The paper addresses a common assumption of elastoplastic modeling: that the recoverable, elastic strain increment is unaffected by alterations of the elastic moduli that accompany loading. This assumption is found to be false for a granular material, and discrete element (DEM) simulations demonstrate that granular materials are coupled materials at both micro- and macro-scales. Elasto-plastic coupling at the macro-scale is placed in the context of thermomechanics framework of Tomasz Hueckel and Hans Ziegler, in which the elastic moduli are altered by irreversible processes during loading. This complex behavior is explored for multi-directional loading probes that follow an initial monotonic loading. An advanced DEM model is used in the study, with non-convex non-spherical particles and two different contact models: a conventional linear-frictional model and an exact implementation of the Hertz-like Cattaneo–Mindlin model. Orthotropic true-triaxial probes were used in the study (i.e., no direct shear strain), with tiny strain increments of  $2 \times 10^{-6}$ . At the micro-scale, contact movements were monitored during small increments of loading and load-reversal, and results show that these movements are not reversed by a reversal of strain direction, and some contacts that were sliding during a loading increment continue to slide during reversal. The probes show that the coupled part of a strain increment, the difference between the recoverable (elastic) increment and its reversible part, must be considered when partitioning strain increments into elastic and plastic parts. Small increments of irreversible (and plastic) strain and contact slipping and frictional dissipation occur for all directions of loading, and an elastic domain, if it exists at all, is smaller than the strain increment used in the simulations.

*Keywords:* Granular material, plasticity, incremental response, stiffness, discrete element method

---

## 1. Introduction

We use discrete element (DEM) simulations to address the micro-scale nature of elastic and plastic deformation in granular materials, and to determine possible coupling of the

---

\*Corresponding to: Donald P. Shiley School of Engineering, University of Portland, 5000 N. Willamette Blvd., Portland, OR, 97203, USA. Email: kuhn@up.edu

Email addresses: kuhn@up.edu (Matthew R. Kuhn), ali.daouadji@insa-lyon.fr (Ali Daouadji)

Preprint submitted to Elsevier

August 1, 2018

plastic and elastic responses and its micro-scale origins. The term “elastic–plastic coupling” is used to describe a dependence of the elastic moduli on alterations in a material’s internal fabric that are brought about by irreversible processes that accompany plastic deformation [25, 50, 20, 36]. Although elastic–plastic coupling is manifested in granular materials as a degradation (and, in some cases, an augmentation) of the elastic moduli, the extent and nature of coupling are open issues, ones that we explore in the paper.

The remainder of this Introduction briefly presents the concepts of thermomechanics that permit a distinction between elastic and reversible deformation increments in coupled materials. The Introduction also explains the role of DEM simulations and the manner in which they are used in the paper, and it briefly describes the two models of contact friction that are used in the simulations. Section 3 focuses on tiny increments of loading and characterizes the micro-scale processes that occur during these increments. The section also presents methods for measuring the small coupling strain increments that are the difference between the elastic and reversible increments. Similar methods are applied in Section 4 to multi-directional probes that determine the constituent parts of the incremental strain — elastic, reversible, plastic, irreversible, and coupled — that result from small loading increments. We find evidence of such elastic–plastic coupling and of the contact-scale dissipation that can enable this coupling, particularly in certain directions of loading. The results are verified for the two models of contact interactions between particles.

### 1.1. Thermomechanics of coupled materials

In this section, we define the elastic and reversible constituents of strain increments, their plastic and irreversible counterparts, and a coupled part that differentiates them. These definitions are presented in the context of continuum thermomechanics [50, 41], of which the first law requires that increments in the internal energy density,  $dU$ , result solely from mechanical stress-work,  $\sigma_{ij}d\varepsilon_{ij}$ , and the external supply of heat,  $dq$ , per unit of volume,

$$dU = \sigma_{ij}d\varepsilon_{ij} + dq \quad (1)$$

where  $d\varepsilon_{ij}$  is a small-strain measure of incremental deformation;  $\sigma_{ij}$  is the corresponding conjugate stress; and density  $U = U(\varepsilon_{ij}^{(e)}, S)$  is taken as a function of the current elastic strain  $\varepsilon_{ij}^{(e)}$  and of the entropy density  $S$ . In this equation, summation applies to the  $i$  and  $j$  subscripts. The cumulative elastic strain can, in principle, be measured as the strain that is recovered upon fully unloading the material to an unstressed reference configuration [25]. Incremental changes in the entropy are separated into reversible and irreversible parts,  $dS = dS^{(r)} + dS^{(i)}$ , of which the reversible part,  $dS^{(r)} = dq/\theta$ , is the quotient of heat input and temperature  $\theta$ . The second law holds that

$$\theta dS \geq dq \quad \text{or} \quad \theta ds^{(i)} = \theta (dS - dS^{(r)}) \geq 0 \quad (2)$$

The Helmholtz free energy density  $F$  is defined by the transformation  $F = U - \theta S$ . Henceforth, we consider only isothermal conditions ( $d\theta = 0$ ), such that

$$dF = dU - \theta dS \quad (3)$$

and combined with Eqs.(1) and (2),

$$\sigma_{ij}d\varepsilon_{ij} - dF = \theta dS^{(i)} \geq 0 \quad (4)$$

which is a measure of dissipation for isothermal conditions. The free energy is assumed a function of the elastic strain  $\varepsilon^{(e)}$  and a set of  $K$  internal variables  $\alpha_k, k = 1, 2, \dots, K$ , that are necessary to fully depict the current state (see [7, 30, 38, 12, 13, 50, 8]):  $F = F(\varepsilon^{(e)}, \alpha_1, \alpha_2, \dots, \alpha_K)$ , noting that an explicit dependence upon temperature is absent for the assumed isothermal conditions. Changes in  $F$  are produced by increments  $d\varepsilon_{ij}^{(e)}$  and  $d\alpha_k$ ,

$$dF = \frac{\partial F}{\partial \varepsilon_{ij}^{(e)}} d\varepsilon_{ij}^{(e)} + \frac{\partial F}{\partial \alpha_k} d\alpha_k \quad (5)$$

with summation over the  $i, j$ , and  $k$  components. The accumulated total strain  $\varepsilon_{ij}$  is the sum of elastic and plastic parts,  $\varepsilon_{ij} = \varepsilon_{ij}^{(e)} + \varepsilon_{ij}^{(p)}$ , the latter, in principle, being the unrecovered strain of a deformed material after it is unloaded to the unstressed reference condition. Combining Eqs. (4) and (5),

$$\left( \sigma_{ij} - \frac{\partial F}{\partial \varepsilon_{ij}^{(e)}} \right) d\varepsilon_{ij}^{(e)} + \sigma_{ij} d\varepsilon_{ij}^{(p)} - \frac{\partial F}{\partial \alpha_k} d\alpha_k = \theta dS^{(i)} \geq 0 \quad (6)$$

as in [7, 38]. This inequality applies to all increments of  $d\varepsilon_{ij}^{(e)}$  and  $d\alpha_k$ , which implies that

$$\sigma_{ij} = \frac{\partial F}{\partial \varepsilon_{ij}^{(e)}} \quad (7)$$

$$\sigma_{ij} d\varepsilon_{ij}^{(p)} - \frac{\partial F}{\partial \alpha_k} d\alpha_k \geq 0 \quad (8)$$

the latter being the dissipation inequality. A stress increment  $d\sigma_{ij}$  is the sum of parts attributed to changes in the elastic strain components and to changes in the internal variables,

$$d\sigma_{ij} = \frac{\partial^2 F}{\partial \varepsilon_{ij}^{(e)} \partial \varepsilon_{kl}^{(e)}} d\varepsilon_{kl}^{(e)} + \frac{\partial^2 F}{\partial \varepsilon_{ij}^{(e)} \partial \alpha_k} d\alpha_k \quad (9)$$

showing that alterations of the internal variables, which typically accompany inelastic loading, can modify the elastic moduli. Hueckel [25] classifies such modifications as elastic hardening or elastic softening, depending on whether the second term in Eq. (9) is aligned or counter-aligned with the first term during a loading increment.

Equation (7) is inverted by using the Gibbs free energy,  $G(\sigma_{ij}, \alpha_1, \alpha_2, \dots, \alpha_K)$ , defined with the transformation  $G = -F + \sigma_{ij} \varepsilon_{ij}^{(e)}$ . By combining Eqs. (1)–(3), and noting that Eq. (4) applies to all increments  $d\sigma_{ij}$ , we have

$$\varepsilon_{ij}^{(e)} = \frac{\partial G}{\partial \sigma_{ij}} \quad (10)$$

With this relation, an increment of strain,  $d\varepsilon_{ij}$ , which is the sum of elastic and plastic increments, is given by

$$d\varepsilon_{ij} = d\varepsilon_{ij}^{(e)} + d\varepsilon_{ij}^{(p)} = \frac{\partial^2 G}{\partial \sigma_{ij} \partial \sigma_{kl}} d\sigma_{kl} + \frac{\partial^2 G}{\partial \sigma_{ij} \partial \alpha_k} d\alpha_k + d\varepsilon_{ij}^{(p)} \quad (11)$$

$$= d\varepsilon_{ij}^{(r)} + d\varepsilon_{ij}^{(c)} + d\varepsilon_{ij}^{(p)} \quad (12)$$

Total strain	$d\varepsilon_{ij}$		
Elastic + plastic strains	$d\varepsilon_{ij}^{(e)}$		$d\varepsilon_{ij}^{(p)}$
Reversible + coupled + plastic strains	$d\varepsilon_{ij}^{(r)}$	$d\varepsilon_{ij}^{(c)}$	$d\varepsilon_{ij}^{(p)}$
Reversible + irreversible strains	$d\varepsilon_{ij}^{(r)}$	$d\varepsilon_{ij}^{(i)}$	

Figure 1: Decomposition of strain increments, from Collins and Housby [8].

In this separation of the total strain increment, proposed by Hueckel, Maier, and Nova [26, 27], the first constituent on the right is the reversible part of the strain increment,  $d\varepsilon_{ij}^{(r)}$ , so named because it would be reversed by a reversal of the stress increment,  $d\sigma_{ij} \leftrightarrow -d\sigma_{ij}$  in the absence of any change in the internal condition of the material, as expressed with the  $\alpha_k$  variables. The coupled constituent  $d\varepsilon_{ij}^{(c)}$  is the portion of the elastic increment attributed to alterations of the elastic moduli that accompany irreversible processes, processes that are brought forth by changes in the internal variables: a coupling of the elastic moduli to the plastic deformation.

Changes of the internal variables are hidden during standard laboratory tests of granular specimens, as they are the consequence of micro-scale phenomena such as crack growth within the grain fragments, asperity fracture at the inter-granular contacts, slip and micro-slip softening of the contact response, and the general rearrangement of particles that accompanies contact slip and micro-slip. Although hidden in laboratory tests, these micro-scale processes are exposed (and can be tracked) in particle-scale numerical simulations. Notably, processes that would otherwise change the internal variables  $\alpha_k$  can be momentarily frozen in simulations, producing a constrained equilibrium state that is nearby a preceding unconstrained state [30, 44] and allowing separate measurements of the small incremental parts  $d\varepsilon_{ij}^{(r)}$ ,  $d\varepsilon_{ij}^{(c)}$ , and  $d\varepsilon_{ij}^{(p)}$ . Our particular simulations were of durable (non-breaking) particles, which could undergo slip and micro-slip at their contacts and be rearranged as a result. These irreversible processes were momentarily frozen in a series of deformation probes (Section 3).

Equation (12) is regrouped as

$$d\varepsilon_{ij}^{(e)} = d\varepsilon_{ij}^{(r)} + d\varepsilon_{ij}^{(c)}, \quad d\varepsilon_{ij}^{(i)} = d\varepsilon_{ij}^{(c)} + d\varepsilon_{ij}^{(p)}, \quad \text{and} \quad d\varepsilon_{ij} = d\varepsilon_{ij}^{(r)} + d\varepsilon_{ij}^{(i)} \quad (13)$$

in which the elastic-plastic coupling part  $d\varepsilon_{ij}^{(c)}$  is a part of the elastic increment, and the irreversible increment  $d\varepsilon_{ij}^{(i)}$  is the part of the total increment  $d\varepsilon_{ij}$  that, in the absence of changes  $d\alpha_k$ , is not reversed by a reversal of the stress increment  $d\sigma_{ij}$  [26, 27]. This decomposition of strains is summarized in Fig. 1, as adapted from [8].

### 1.2. DEM modeling in relation to a thermomechanics framework

Discrete particle (DEM) simulations were used to measure strain increments for different directions of loading and to decompose an increment of total strain into the various parts from which it is derived: the reversible, irreversible, elastic, plastic, and coupled parts. We also used simulations to gain an understanding of the underlying micro-scale mechanisms that contribute to bulk deformation and of contact-scale frictional dissipation. Because micro-scale information and more general boundary conditions are accessible with DEM simulations, they can expose granular behavior in ways that are not easily achieved with

laboratory testing. Specifically, four advantages of DEM simulations were exploited in our simulations:

1. After a granular assembly has been created and loaded to a given state, this state and all of its micro-data (particle positions, contact forces, Jäger-equivalent contact history, etc.) can be saved. This saved state — which Alonso-Marroquín [2] calls a numeric “clone” — constitutes a consistent reference state for subsequent loading probes that precisely captures (to within machine precision) the essential micro-scale condition of the system.
2. In performing loading probes, DEM codes permit control of any combination of six components of the stress and strain tensors or any six linearly independent combinations of stress and strain — loading conditions that would require multiple sample preparations and even different testing apparatus in a physical laboratory [32]. Such multi-directional probes are used to fully characterize elastic–plastic coupling (Section 4).
3. One can extract the bulk elastic energy and the bulk frictional dissipation from their micro-scale origins within a material (Section 3.1). The “stored” energy is computed at each inter-particle contact, and the total contact energy of all contacts is a direct measure of the Helmholtz energy  $F$  and any incremental change  $dF$ .

Micro-scale contact frictional dissipation can also be obtained from these probes. Dissipation in granular materials can result from frictional slip, frictional micro-slip, plastic deformation of the particles, particle fracture, and viscous drag of the particles as they move through (or relative to) a pore fluid. Our focus is on the slow, quasi-static loading of uncemented dry materials at low confining pressure (the mean stress, defined as the negative of 1/3 of the first stress invariant) and with durable particles, for which frictional contact slip and micro-slip are the dominant dissipation mechanisms. As such, viscous damping is kept as small as is necessary to maintain computational stability, so that dissipation results solely from frictional slip and micro-slip at the contacts (Section 3.1 and Appendix B).

4. By momentarily suspending contact slip and micro-slip during a loading probe, DEM simulations can be used for distinguishing the reversible and irreversible parts of a total strain increment. When compared with a conventional, unconstrained probe, one can decompose the total increment  $d\varepsilon_{ij}$  into the source parts of Eqs. (12) and (13) (see the Types 2 and 3 probes of Section 3).

Although simulations offer these advantages, the results depend, however, upon the model that is ascribed to the individual contacts, an issue that is addressed in our study.

### 1.3. Two contact models: linear-frictional and Cattaneo–Mindlin

The deformation of a granular material with durable grains depends upon the material’s contact-scale behavior, and two contact models are used in this study: a standard linear-frictional contact model and a Hertz–Mindlin model, which we will call the *Cattaneo–Mindlin* contact. The purpose is to ascertain the bulk incremental behavior and its relation to the particular contact model. Both models are elastic with respect to movements that are normal to the particles’ surfaces: the first model has a linear force-displacement relation for normal

movements; the second has a non-linear Hertz-type relation. Moreover, because the contact loads and indentations are small, the contact zones are finite but small, and the behavior of a single contact is unaffected by the loading of more distant contacts on the same particle (see [21] for the case of large indentations).

For tangential movements, the standard linear-frictional model uses a linear force-displacement relation, with elastic “spring” stiffnesses  $k^n$  and  $k^t$  in the normal and tangential directions. The behavior is entirely elastic when  $|\mathbf{f}^t| < \mu f^n$ , where  $f^n$  and  $\mathbf{f}^t$  are the normal and tangential forces, and  $\mu$  is the contact friction coefficient. Contact behavior can become partially or wholly plastic (i.e., with slip) when the friction limit is reached,  $|\mathbf{f}^t| = \mu f^n$ , and the frictional loss (energy dissipation) can be computed for a sliding contact. Details of this model’s incremental behavior are given in Appendix A.

A second set of simulations used a more realistic contact model having a Hertz-like and elastic normal contact stiffness and an exact representation of the corresponding inelastic tangential response. Hertz contact is recognized as an improved representation of elasto-frictional particle interaction, but because of its coding complexities and computational demands, a faithful implementation of Hertz contact, which should include micro-slip, is rarely fulfilled in DEM simulations. Two isotropic elastic spheres, when pressed together, touch within a circular contact patch between the particles’ two surfaces. The corresponding inelastic tangential force-displacement behavior is modeled with Cattaneo–Mindlin theory [39]. When a small tangential force is applied between the two spheres, frictional slip does not occur uniformly across the full contact patch, instead, the slip is confined to an outer annular ring with a width that depends on the applied tangential force and on the force (or displacement) history. Such annular “micro-slip” produces frictional dissipation within the contact patch, which can give way to full sliding of the entire contact patch when the tangential force  $|\mathbf{f}^t|$  reaches the limit  $\mu f^n$  (i.e., the outer slip cone  $|\mathbf{f}^t| = \mu f^n$  in Fig. A.11c). Because micro-slip and dissipation can occur inside this slip cone, the contact can exhibit plastic and incrementally nonlinear behaviors when the tangential force *is less than* the friction limit (when  $|\mathbf{f}^t| < \mu f^n$ ). This response is akin to elasto-plastic strain hardening at the contact scale. The resulting incremental contact behavior can be elastic, micro-slip, or full slip, depending upon the direction of loading. More commonly, approximate implementations of the Hertz contact simply use a tangential stiffness that is proportional to the normal force and not upon the directions of the normal and tangential movements [9, 37]. Such implementations do not permit frictional dissipation in the form of micro-slip and can result in an unfortunate and physically inadmissible infusion of energy during close cycles of contact movement [18]. Details of the exact implementation of the Cattaneo–Mindlin model used in this study are described in Appendix A and the references therein.

The two contact models can be summarized in the context of a thermomechanic framework. Elastic energy is stored within the contacts and frictional dissipation is produced by slip and micro-slip, and both incremental consequences of the stress-work  $\sigma_{ij} d\varepsilon_{ij}$  can be audited throughout a DEM simulation. Besides the shapes of the particles and their arrangements (i.e., the material’s internal geometric fabric), the internal condition of a material with simple linear-frictional contacts is additionally described by the current normal and tangential forces at each contact. A material with Cattaneo–Mindlin contacts requires this information and more, including the full Jäger equivalent-loading information of each contact (Appendix A). All of this information can be stored in DEM files, so that each probe in a series of probes can retrieve the information, and that each probe is initiated from the same internal condition.

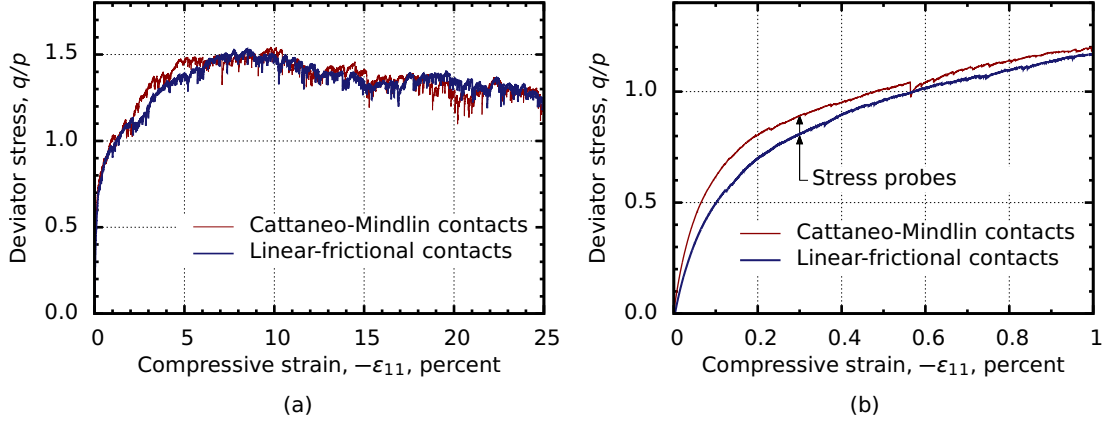


Figure 2: Stress and strain during DEM simulation of triaxial compression at constant mean stress with 10,648 non-convex sphere-cluster particles ( $p_0 = 100$  kPa). Stress probes in Sections 3 and 4 were initiated from a strain of 0.3%.

## 2. Monotonic triaxial compression

We used a series of slow, quasi-static DEM simulations to study the incremental response of a granular assembly. The assembly was a cubical box filled with 10,648 smooth non-convex sphere-cluster particles and contained within periodic boundaries. The particles' shape, sizes, and arrangement were calibrated to simulate the behavior of a fine-grain poorly-graded medium-dense sand (Nevada Sand [4, 35]; model details are described in Appendix B). The assembly was large enough to capture the average material behavior but sufficiently small to prevent meso-scale localization, such as shear bands. The initial particle arrangement was isotropic with a confining pressure,  $-\frac{1}{3}(\sigma_{11} + \sigma_{22} + \sigma_{33})$ , of 100 kPa.

Although it is inconsistent with the quasi-static hypothesis, DEM results can depend upon the loading rate — an unfortunate dependence which is infrequently discussed in a candid manner in the DEM literature. To mitigate such rate dependence, a slow loading rate and other measures were taken, assuring that the simulations were nearly quasi-static. Because of their importance in the current study, computational essentials are detailed in Appendix B, which also describes quantitative indicators verifying the quasi-static nature of the simulations.

Figure 2 shows the results of drained constant- $p$  triaxial compression, in which the  $x_1$  width of the assembly was reduced at constant rate  $\dot{\varepsilon}_{11}$  while adjusting the lateral widths to maintain a constant mean stress  $p$  of 100 kPa. Henceforth, this type of axisymmetric triaxial loading is referred to as constant- $p$  loading. Results are shown for the two contact models: linear-frictional and Cattaneo–Mindlin. The initial, small-strain modulus differed for the two simulations (initial moduli of elasticity  $E$  of 83 GPa and 111 GPa for the linear-frictional and Cattaneo–Mindlin models respectively). Better agreement of these small-strain moduli could be obtained, of course, by further tuning the contact stiffnesses, but the results are considered satisfactory for the current study. Results with the two contact models were quite similar, however, when the strains were larger than 0.5%. This similarity indicates that the large-strain monotonic behavior is less sensitive to the details of the contact model, provided that different models incorporate the same friction coefficient  $\mu$ .

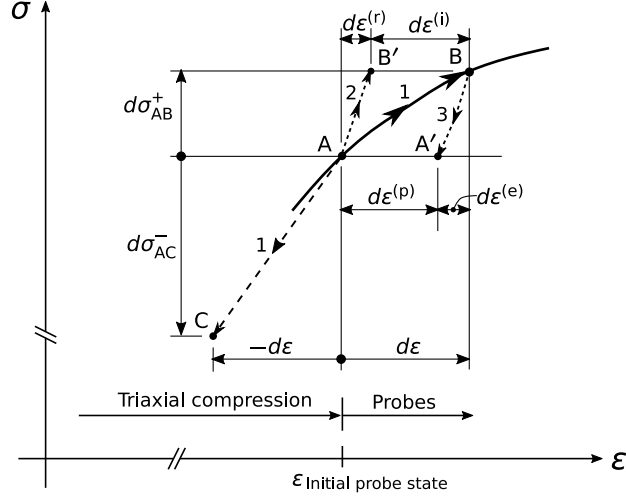


Figure 3: Three pairs of loading probes. Numerals correspond to the Type 1, Type 2, and Type 3 probes that are summarized in Table 1.

### 3. Stress probes, dissipation, and coupled response

DEM simulations were used to explore micro-scale conditions at the contacts and to quantify the elastic, plastic, reversible, irreversible, and coupled parts of strain increments. To these ends, we conducted three types of stress and strain probes: (1) loading-retrogression pairs, (2) loading and reversible loading pairs, and (3) loading-unloading pairs. The three types of probes are illustrated in Fig. 3, summarized in Table 1, and described in separate sections below. The loading-retrogression pairs (Type 1) involved a loading probe and a strain-reversal (retrogression) probe and were used to compare the micro-scale changes in contact behavior during bulk strains applied in opposite directions. The loading and reversible loading pairs (Type 2) were used to determine the reversible and irreversible parts of a strain increment; whereas, loading-unloading pairs (Type 3) produced a small closed path in stress-space and were used to determine the elastic and plastic parts of a strain increment. Simulations with the two contact models, Cattaneo–Mindlin and linear-frictional, were also compared with these probes.

The initial, reference states for the probes were established with drained monotonic constant- $p$  triaxial compression, in which the mean stress  $p$  was maintained constant during axial ( $x_1$  direction) loading (Fig. 2). At several strains, we saved the entire state of all particles and contacts, so that the different deformation probes started from the same reference state — the “initial probe state” (point A in Fig. 3). For all three types of probe-pairs, the *loading* probe was simply a continuation of the previous triaxial compression: starting from the initial probe state, the strain  $\varepsilon_{11}$  was reduced (compressed) by an additional  $2 \times 10^{-6}$  (path A–B in Fig. 3), in a continuation of constant- $p$  compression. A similar strain increment of  $2 \times 10^{-6}$  was used with all three types of probes and in various loading directions. Halving or doubling the strain increment or strain rate had minimal effect on the results (Appendix A).



Table 1: Summary of simulation probes.

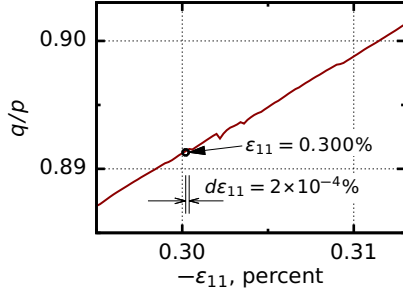
Type	Probe pairs	Fig. 3	Description	
1	Loading & retrogression	A-B A-C	reference loading increment retrogression (strain-reversal) increment	$d\epsilon \rightarrow d\sigma_{AB}^+$ $-d\epsilon \rightarrow d\sigma_{AC}^-$
2	Loading & reversible loading	A-B A-B'	reference loading increment reversible increment	$d\epsilon \rightarrow d\sigma_{AB}^+$ $d\sigma_{AB}^+ \xrightarrow{\mu \rightarrow \infty} d\epsilon^{(r)}$ $d\epsilon^{(i)} = d\epsilon - d\epsilon^{(r)}$
3	Loading & unloading	A-B B-A'	reference loading increment unloading increment	$d\epsilon \rightarrow d\sigma_{AB}^+$ $-d\sigma_{AB}^+ \rightarrow -d\epsilon^{(e)}$ $d\epsilon^{(p)} = d\epsilon - d\epsilon^{(e)}$

### 3.1. Loading and retrogression (Type 1) probes with Cattaneo–Mindlin contacts

The loading phase of these probes was begun from an initial probe state (the increment AB in Fig. 3). For the results of this section, the loading was of continued constant- $p$  triaxial compression with a strain increment of  $d\epsilon_{11} = -2 \times 10^{-6}$ ; whereas, in Section 4 the loading phase was conducted in other directions. We noted and stored all three components of the strain during this loading probe — components  $d\epsilon_{11}$ ,  $d\epsilon_{22}$ , and  $d\epsilon_{33}$  — and starting again from the same initial probe state (point A), we precisely reversed these strain components for the *retrogression* (strain-reversal) probe AC, with the intent of determining the alterations of micro-scale contact movements that were produced by strain increments in opposite directions.

Figure 4 shows results for the loading and retrogression probes that originated at strain  $\epsilon_{11} = -0.3\%$  in the simulation with Cattaneo–Mindlin (i.e., Hertz-type) contacts. This initial probe state was during the strain-hardening phase, when deviator stress was about 55% of the peak strength (Fig. 4a). As expected, the stiffness was much smaller during loading than during retrogression, with moduli  $d\sigma_{11}/d\epsilon_{11}$  of 12.7 GPa and 109 GPa, respectively (Fig. 4b). During the loading probe, the material dilated slightly, at rate  $dv/|d\epsilon_{11}| = 0.12$ .

By post-processing the micro-scale data, the condition of each Cattaneo–Mindlin contact — elastic, micro-slip, or full slip — was determined during loading and retrogression (see Section 1.3 and Appendix A). Nine transitions are possible among these three contact conditions, and the table in Fig. 4c gives the fractions of contacts that transitioned in each manner between loading (rows) and retrogression (columns). For example, 11.2% of all contacts were elastic during the loading increment but exhibited micro-slip during the strain-reversal increment. Eight of the nine possible pairings occurred among the contacts. Consider, for example, the 29.0% of contacts that were sliding (full slip) during loading. Of these sliding contacts, 23% ( $= 0.066/0.290$ ) were also sliding during the strain-reversal (retrogression) probe, 67% transitioned to micro-slip, and only 10% became fully elastic. Of the 12.7% of contacts that were elastic during loading, 88% transitioned to micro-slip during the retrogression probe. Of the contacts that were undergoing micro-slip, only 13% transitioned to an elastic condition during the strain-reversal probe, and a small number had transitioned to full slip. In other words, a reversal of strain does not necessarily reverse (toggle) the mode of a contact’s movement: some contacts that were sliding or in micro-slip continued in these modes when the strain was reversed. The only transition that was not observed was the



(a)

	Loading probe	Retrogression probe
$d\varepsilon_{11}$	$-2.00 \times 10^{-6}$	$2.00 \times 10^{-6}$
$d\varepsilon_{22}$	$1.12 \times 10^{-6}$	$-1.12 \times 10^{-6}$
$d\varepsilon_{33}$	$1.12 \times 10^{-6}$	$-1.12 \times 10^{-6}$
$d\sigma_{11}$	-25.4 Pa	218 Pa
$d\sigma_{22}$	13.1 Pa	-25.1 Pa
$d\sigma_{33}$	12.4 Pa	-23.8 Pa

(b)

		Retrogression probe			Loading totals
		Elastic	Micro-slip	Slip	
Loading probe	Elastic	0.015	0.112	0.000	0.127
	Micro-slip	0.076	0.506	0.001	0.583
	Slip	0.030	0.194	0.066	0.290
Retrogression totals		0.121	0.812	0.067	1.000

(c)

Figure 4: Results of loading and retrogression (strain-reversal) Type 1 probes, starting at strain  $\varepsilon_{11} = -0.3\%$  with Cattaneo–Mindlin contacts. (a) stress-strain during constant- $p$  triaxial compression, with the small probe  $d\varepsilon_{11}$  (see Fig. 2 for the full range of stress and strain); (b) strain and stress increments during loading (AB) and strain-reversal (AC) probes; and (c) fractions of contacts that transition among the three contact conditions (elastic, micro-slip, and slip) between the loading (AB) and strain-reversal (AC) probes.

unlikely case of a contact that was elastic during loading but transitioned to full slip during retrogression.

Considering the small magnitude of the strain increment ( $|d\varepsilon_{11}| = 2 \times 10^{-6}$ ), these results suggest that a zone of purely reversible response (or a cone, in the sense of Darve [16]) does not exist during the strain-hardening phase. Our results with linear-frictional contacts are given in Section 3.4, where a similar conclusion is made. This difficulty of distinguishing a finite zone of purely reversible response has also been noted in the simulations of ductile powder compacts [23], was anticipated by Hill [24] for multi-slip crystal plasticity, and is modeled in the generalized plasticity of Mroz et al. [40]. The results in this section are for a single pair of loading and retrogression increments. These results, by themselves, do not refute the possibility of an elastic zone (indeed, the generalized plasticity of Mroz admits an elastic zone of zero measure at the interface of adjacent plastic zones). However, the multi-direction probes of Section 4 show that small plastic (and irreversible) increments occur for all directions of loading.

As a further investigation of contact behavior during these small increments of loading and retrogression, we compared the *directions* of the contact movements during the two probes that began at strain  $\varepsilon_{11} = -0.3\%$  (again, with simulations having Cattaneo–Mindlin contacts). Focusing on the tangential movements  $d\xi$  of pairs of particles at their contacts, the radial bars in Fig. 5 show the directions in which tangential movement occurred during the strain-reversal (retrogression) probe when compared with the directions during the loading probe for the same contacts. The arrow pointing to the right represents the movement

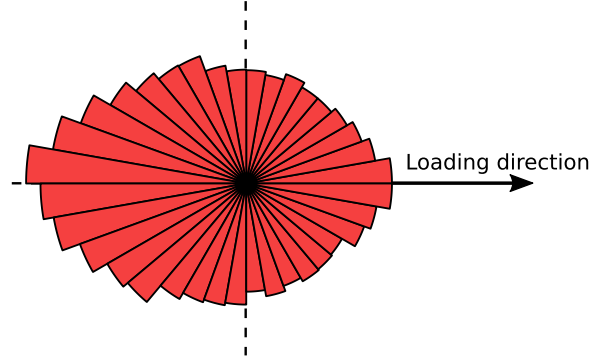


Figure 5: Comparison of the directions of tangential contact movements  $d\xi$  during loading and retrogression (strain-reversal) for Type 1 probes, initiated at at the reference strain  $\varepsilon_{11} = -0.3\%$  with Cattaneo–Mindlin contacts. Each radial bar represents the number of contacts that, although moving toward the right during loading, were moving in the bar’s direction during a reversal of the strain.

direction during loading (the movement direction of each contact during loading has been rotated to this arrow’s direction so that their corresponding retrogression directions can be compared). Bar sizes indicate the relative numbers of contacts with a given movement direction. The figure shows that during strain-reversal, the directions of contact movement are not simply reversed from their original loading directions: the movements are not strongly directed toward the left in this figure. In fact, there is only a small correlation between the directions of contact movements for the two opposite directions of bulk strain, with only a small bias toward a reversal of the movements when strain is reversed. Quite simply, micro-scale contact movements are not reversed by a reversal of the macro-scale deformation.

To better understand the degree of irreversible behavior during the retrogression probe, we also audited energy changes, measuring the increments in work density attributed to elastic deformations at the contacts and to dissipative, frictional micro-slip and slip at the contacts. For the loading probe, the increment of stress-work density  $\sigma_{ij}d\varepsilon_{ij}$  was a positive  $0.82 p d\varepsilon_{11}$  ( $p$  being the mean stress of 100kPa, and  $d\varepsilon_{11}$  being the positive increment  $2 \times 10^{-6}$ ); and since deformation was precisely reversed during the retrogression probe, the corresponding increment was a negative  $-0.82 p d\varepsilon_{11}$ . During the loading probe, frictional contact dissipation was  $0.79 p d\varepsilon_{11}$ , accounting for about 96% of the stress-work, the remaining 4% being a small change in the contacts’ elastic energy. Although frictional contact dissipation was less during the reversal probe (about  $0.13 p d\varepsilon_{11}$ ), the frictional dissipation was still quite substantial, about 17% of the stress-work, while the elastic energy was reduced by  $-0.95 p d\varepsilon_{11}$ . In short, the material exhibited frictional dissipation in the form of contact slip and micro-slip during both loading and retrogression, even with the very small strain increment of  $2 \times 10^{-6}$ .

### 3.2. Loading and reversible loading (Type 2) probes with Cattaneo–Mindlin contacts

With Type 2 probes, we determined the amount and direction of the reversible and irreversible parts of a strain increment, using a technique pioneered by Calvetti and his co-workers [6, 47]. As we have seen, frictional contact dissipation occurs both during loading and during a reversal of the loading strain (retrogression). Because such frictional dissipation indicates that deformation is only partially reversible during both loading and retrogression,

Table 2: Results of loading and reversible (Type 2) probes, starting at strain  $\varepsilon_{11} = -0.3\%$  with Cattaneo–Mindlin contacts. Reversible strains were determined by artificially suppressing contact sliding.

Probe	Strain component	Reversible $d\varepsilon^{(r)}$	Irreversible $d\varepsilon^{(i)}$	Total $d\varepsilon$
Loading	$d\varepsilon_{11}$	$-2.94 \times 10^{-7}$	$-17.06 \times 10^{-7}$	$-20.00 \times 10^{-7}$
	$dv$	$2.00 \times 10^{-7}$	$0.31 \times 10^{-7}$	$2.31 \times 10^{-7}$

we can not separate the loading increments into reversible and irreversible parts by simply comparing pairs of loading-retrogression (Type 1) probes or by using closed stress-paths (the latter are Type 3 probes, which are considered below for another purpose). To determine the reversible part of deformation, we conducted a “reversible probe” (AB’ in Fig. 3 and Table 1) by replicating the same *stress increment* as during loading (increment  $d\sigma_{AB}^+$ ), but by momentarily intervening (for the duration of the strain increment) and preventing micro-slip and slip by assigning a large friction coefficient to the contacts (i.e.,  $\mu = 50$ ). That is, we first determined the stress increment  $d\sigma_{AB}^+$  that resulted from unadulterated loading with  $\mu = 0.55$  (the stresses reported in Fig. 4b), and then we produced this same stress increment with  $\mu = 50$ . The latter strain increments were free of slip and micro-slip and were entirely the result of elastic contact movements: these strain increments are the reversible parts  $d\varepsilon^{(r)}$  in Eqs. (11)–(12), and the irreversible parts  $d\varepsilon^{(i)}$  are the differences  $d\varepsilon - d\varepsilon^{(r)}$ , as in Eq. (13<sub>3</sub>).

The results for a probe of constant- $p$  triaxial compression are presented in Table 2, showing the reversible and irreversible strain parts of the loading probe. Both axial  $d\varepsilon_{11}$  and volumetric  $dv$  strains are reported. The table shows that over 85% of the loading strain  $d\varepsilon_{11}$  was irreversible. During loading, both reversible and irreversible parts of volume change,  $dv^{(r)}$  and  $dv^{(i)}$ , were dilative, with most of the incremental dilation being reversible.

### 3.3. Loading and unloading (Type 3) probes with Cattaneo–Mindlin contacts

With the final variant of probes, we used conventional pairs of loading and unloading increments, producing a tiny closed path in stress-space (Fig. 3 and Table 1). This conventional technique is used in laboratory and numerical testing to determine the elastic and plastic parts of a strain increment (for example, [5, 3, 45, 31, 1]). The loading probe AB is detailed in Fig. 4b for the initial probe state at strain  $\varepsilon_{11} = -0.3\%$ , and this loading increment advanced the compressive strain  $d\varepsilon_{11}$  by  $2 \times 10^{-6}$  while maintaining constant mean stress, ending with the stress increment  $d\sigma_{AB}^+$ . The unloading probe BA’ was a reversal  $-d\sigma_{AB}^+$  of the *stress* produced during forward loading, resulting in the elastic strain increment  $-d\varepsilon^{(e)}$  (that is, we reversed the stresses shown in the bottom half of the loading column in Fig. 4b). This elastic increment includes a reversible part — the increment  $(\partial^2 G / \partial \sigma_{ij} \partial \sigma_{kl}) d\sigma_{kl}$  in Eq. (11) — and a coupled part that arises from changes in the elastic moduli that accompany the plastic deformation. The coupling part is associated with the slip and micro-slip of contacts and small particle rearrangements, which occur during both loading and unloading. With the pair of probes, we determined the elastic and plastic strain increments, as given on the left of Eq. (11).

Table 3 summarizes the elastic and plastic strain increments for a probe of constant- $p$  compression and also includes the reversible and irreversible parts taken from Table 2. The table reveals a slight difference between the reversible and elastic increments and between the irreversible and plastic increments, and this difference is the coupled part in Eqs. (12)

Table 3: Results of loading and unloading (Type 3) probes, starting at strain  $\varepsilon_{11} = -0.3\%$  with Cattaneo–Mindlin contacts. Results of Type 2 probes are also shown.

Decomposition	Strain components	
	$d\varepsilon_{11}$	$dv$
Reversible, $d\varepsilon_{ij}^{(r)}$	$-2.94 \times 10^{-7}$	$2.00 \times 10^{-7}$
Irreversible, $d\varepsilon_{ij}^{(i)}$	$-17.06 \times 10^{-7}$	$0.31 \times 10^{-7}$
Elastic, $d\varepsilon_{ij}^{(e)}$	$-2.57 \times 10^{-7}$	$2.37 \times 10^{-7}$
Plastic, $d\varepsilon_{ij}^{(p)}$	$-17.43 \times 10^{-7}$	$-0.06 \times 10^{-7}$
Coupled, $d\varepsilon_{ij}^{(c)}$	$0.37 \times 10^{-7}$	$0.37 \times 10^{-7}$
Total, $d\varepsilon_{ij}$	$-20.00 \times 10^{-7}$	$2.31 \times 10^{-7}$

Table 4: Results of loading and retrogression (strain-reversal) Type 1 probes, starting at strain  $\varepsilon_{11} = -0.3\%$  with linear-frictional contacts. Transitions across the two contact conditions (elastic and slip) are shown between the loading (AB) and strain-reversal (AC) probes.

		Retrogression		Loading totals
		Elastic	Slip	
Loading	Elastic	0.878	0.000	0.878
	Slip	0.111	0.011	0.122
Retrogression totals		0.989	0.011	1.000

and (13). Reversible and recoverable (elastic) strain increments are not equivalent, as a small coupled part  $d\varepsilon_{ij}^{(c)}$  accompanies loading. Although the coupled axial strain part  $d\varepsilon_{11}^{(c)}$  may seem small, the coupled part of volume change  $dv^{(c)}$  was larger when compared with its elastic and plastic parts. These results contrast with those of Wan and Pinheiro [49], who found no difference between plastic and irreversible increments of strain in their simulations of triaxial compression with sphere assemblies. Our result is not unexpected, however, since frictional contact dissipation, an irreversible process that can contribute to the total strain increment, was found to occur during loading, during unloading, and during strain-reversal, indicating that the unloading increment is not entirely irreversible. In Section 4, we will see that the small elastic-plastic coupling revealed in Table 3 is for a probe direction that *minimizes* such coupling, and more significant coupling occurs in other loading directions. Also note that the reversible, coupled, and plastic parts are not aligned, but rather occur in different directions with different relative rates of dilation, a possibility suggested by Hueckel [25] and explored for other loading directions (Section 4).

### 3.4. Stress probes with linear-frictional contacts

Similar results were also obtained in simulations using the simpler linear-frictional contact model (see Figs. A.11a and A.11b). Table 4 gives results for the initial probe state  $\varepsilon_{11} = -0.3\%$ , which is during the strain-hardening phase of loading, when the deviator stress had reached about 50% of the peak strength (Fig. 2). The table gives the fraction of elastic and slip contacts during the tiny loading and retrogression probes (again, a  $d\varepsilon_{11}$  of  $-2 \times 10^{-6}$ ). Similar to Fig. 4c, the table presents these fractions of contacts in terms of the transitions of

Table 5: Results of loading and reversible (Type 2) probes, starting at strain  $\varepsilon_{11} = -0.3\%$  with linear-frictional contacts. Reversible strains were determined by artificially suppressing contact sliding.

Probes	Strain	Reversible $d\varepsilon_{ij}^{(r)}$	Irreversible $d\varepsilon_{ij}^{(i)}$	Coupled $d\varepsilon_{ij}^{(c)}$	Total $d\varepsilon_{ij} = d\varepsilon_{ij}^{(r)} + d\varepsilon_{ij}^{(i)}$
Types 2 & 3	$d\varepsilon_{11}$	$-4.21 \times 10^{-7}$	$-15.79 \times 10^{-7}$	$0.43 \times 10^{-7}$	$-20.00 \times 10^{-7}$
	$dv$	$1.56 \times 10^{-7}$	$-0.71 \times 10^{-7}$	$0.33 \times 10^{-7}$	$0.85 \times 10^{-7}$

elastic and slip modes between loading and retrogression (strain-reversal). Only four transitions are applicable between the two modes, and three of these occurred. For example, of the 11.1% of contact that were sliding during loading, about 10% ( $= 1.1\%/11.1\%$ ) continued to slide during the strain-reversal probe. As with the more complex Cattaneo–Mindlin contacts, some contacts continued to slip during a reversal of strain.

Types 2 and 3 probes were also performed with linear-frictional contacts. The results of loading and retrogression (Type 2) probes are shown in Table 5. The results are similar to those with Cattaneo–Mindlin contacts (Section 3.2): about 79% of the loading increment  $d\varepsilon_{11}$  is irreversible; the reversible part of volume change was dilative; and the irreversible part of volume change was contractive (see Section 5 for further discussion). With loading-unloading (Type 3) probes, also included in Table 5, the directions of the elastic and plastic increments were the same as those with Cattaneo–Mindlin contacts (as in Table 3), and small coupled strain increments accompany the closed path in stress-space.

#### 4. Multi-directional elastic-plastic coupling

The results discussed above are exclusively for axisymmetric triaxial conditions, in which the initial probe state was established with constant- $p$  triaxial compression ( $\varepsilon_{11} < 0$ ) and in which the subsequent triaxial probes were conducted with equal lateral strains,  $d\varepsilon_{22} = d\varepsilon_{33}$ . We now consider multi-directional (i.e., true-triaxial) probes that began from initial probe states that were established, as in the previous section, with constant- $p$  triaxial compression. One set of probes was conducted within the deviatoric pi-plane of isochoric or isobaric strain increments; another set of probes was of generalized triaxial loading within the Rendulic plane of volumetric and deviatoric strain increments. With each series of probes (in the pi-plane or Rendulic plane), we conducted over 50 probes in different directions, and both Types 2 and 3 probes were used to measure the elastic, plastic, and coupled parts of the total strain increment for each probe direction.

Figure 6 shows strain results within the pi-plane for isochoric (undrained) probes that were initiated at strain  $-\varepsilon_{11} = 0.3\%$  for the assembly with Cattaneo–Mindlin contacts. These results are for the early stage of strain hardening at which the material had reached 55% of the peak strength. Again, this initial probe state was reached with constant- $p$  triaxial compression (see Fig. 2). Probes of *equal strain-increment magnitude* were used for each loading direction, with  $|d\varepsilon_{ij}| = (d\varepsilon_{11}^2 + d\varepsilon_{22}^2 + d\varepsilon_{33}^2)^{1/2} = 2 \times 10^{-6}$ . The pi-plane strains in Fig. 6a have been scaled so that strain increments of equal magnitude are equidistant from the origin. The upward vertical direction,  $\theta = 0^\circ$ , is for continued isochoric triaxial compression ( $d\varepsilon_{11} < 0$ ,  $d\varepsilon_{22} = d\varepsilon_{33} = -\frac{1}{2}d\varepsilon_{11}$ ); and the downward direction,  $\theta = 180^\circ$ , is for triaxial extension ( $d\varepsilon_{11} > 0$ ,  $d\varepsilon_{22} = d\varepsilon_{33} = -\frac{1}{2}d\varepsilon_{11}$ ). The horizontal directions,  $\theta = 90^\circ$  and  $270^\circ$ , correspond to transverse deviatoric loading ( $d\varepsilon_{11} = 0$ ,  $d\varepsilon_{22} = -d\varepsilon_{33}$ ).

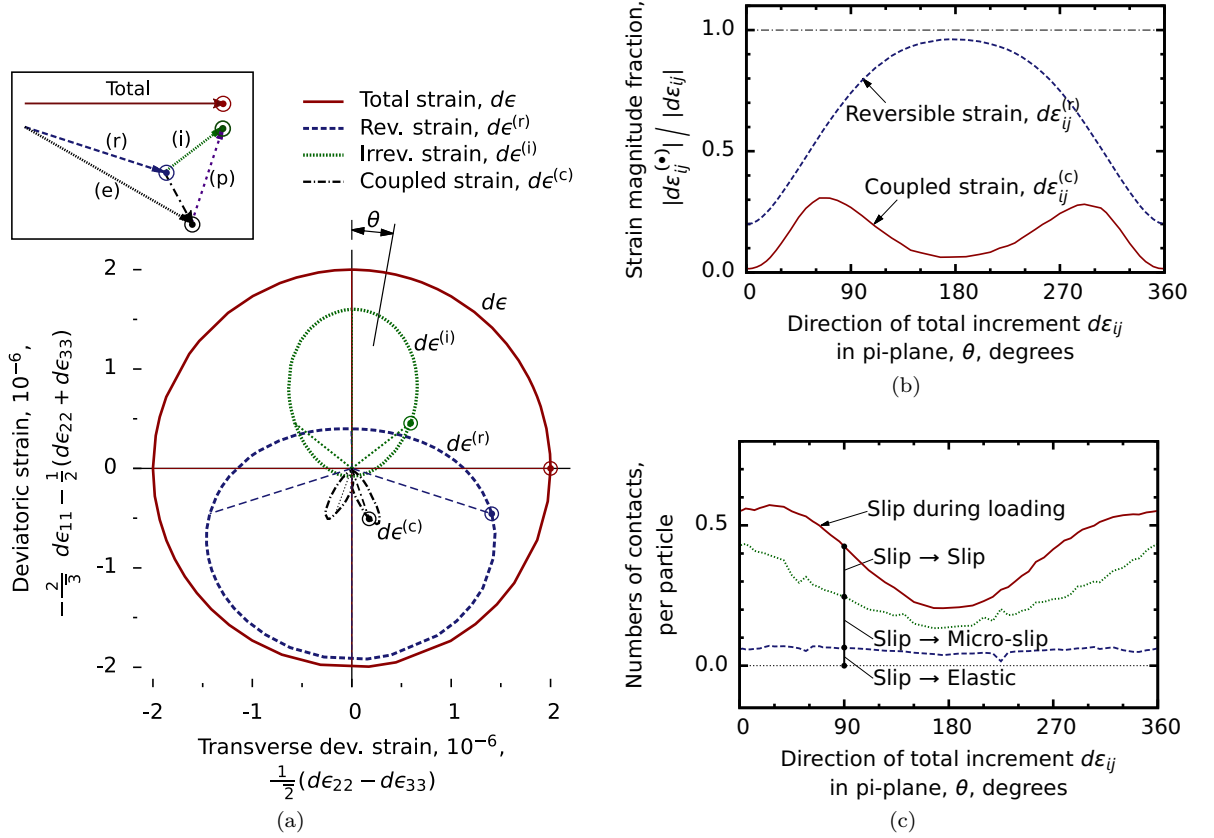


Figure 6: Isochoric probes of magnitude  $|d\epsilon_{ij}| = 2 \times 10^{-6}$  at strain  $\epsilon_{11} = -0.3\%$  for the assembly with Cattaneo-Mindlin contacts: (a) pi-plane of deviatoric and transverse-deviatoric strain increments; (b) magnitudes of the reversible and coupled strain increments relative to the magnitude of the total strain increment; and (c) transitions for the loading and unloading probes among the set of contacts that were slipping during loading. Dots “ $\odot$ ” are for a total increment  $d\epsilon_{ij}$  of transverse deviatoric loading ( $\theta = 90^\circ$ ), and the inset at the top of Fig. 6a shows the addition of the  $d\epsilon_{ij}^{(r)}$  and  $d\epsilon_{ij}^{(i)}$  vectors.

Each closed line in Fig. 6 is a locus of over 50 strain increments — lines of total  $d\epsilon_{ij}$ , reversible  $d\epsilon_{ij}^{(r)}$ , irreversible  $d\epsilon_{ij}^{(i)}$ , and coupled  $d\epsilon_{ij}^{(c)}$  — for different isochoric combinations (directions) of the strain increments  $d\epsilon_{11}$ ,  $d\epsilon_{22}$ , and  $d\epsilon_{33}$ . During the stage of early strain hardening that is represented in the figure, the reversible and irreversible parts are of similar magnitude. As an example, the “ $\odot$ ” symbols in Fig. 6a show the incremental parts of a total strain increment of transverse deviatoric loading (i.e., for a total increment  $d\epsilon_{ij}$  have  $\theta = 90^\circ$ , which is an increment that is orthogonal to both the volumetric and deviatoric directions). For this particular loading direction, the inset in the top left corner of Fig. 6a shows how the various parts combine to form the total increment  $d\epsilon_{ij}$  (the small vector in the middle of the inset is the coupled part  $d\epsilon_{ij}^{(c)}$ ). The inset shows the distinctly different directions of the reversible, irreversible, elastic, plastic, and coupled parts. In the main plot of Fig. 6a, the locus of coupled strain increments appears as two lobes below the horizontal axis, corresponding to increments roughly in the direction of triaxial extension. Not only is coupling present, but

the magnitude  $|d\varepsilon_{ij}^{(c)}|$  is, for some loading directions, significant when compared with the reversible and irreversible parts. For certain loading directions, the coupled magnitude is about 30% of the total increment  $|d\varepsilon_{ij}|$ . We also note that in no deviatoric loading direction is the irreversible increment (or, for that matter, the plastic increment) zero, as the  $d\varepsilon_{ij}^{(i)}$  locus fully envelops the origin.

The significance of elastic-plastic coupling during deviatoric (pi-plane) loading is also shown in Fig. 6b, which gives the fractions  $|d\varepsilon_{ij}^{(c)}|/|d\varepsilon_{ij}|$  and  $|d\varepsilon_{ij}^{(r)}|/|d\varepsilon_{ij}|$  of the magnitudes of coupled and reversible parts relative to the total strain increment. The results for different directions  $\theta$  of the total increment  $d\varepsilon_{ij}$  demonstrate that elastic strains are not entirely reversible, particularly for probe directions that are oblique to the initial loading direction ( $\theta = 0^\circ$ ), as these oblique directions produce significant coupled increments. To place the results of Section 3 in the context of those in Fig. 6, the probes of the previous section were strictly of triaxial compression (i.e., in the upward direction,  $\theta = 0^\circ$ , of Fig. 6a). Of the  $360^\circ$  of loading directions, the coupled increments are *smallest* for probes that continue in this original (upward) direction of loading.

The micro-scale origin of elastic-plastic coupling is the subject of Fig. 6c, which quantifies the transitions of the contacts' conditions for the loading and unloading phases of a closed Type 2 path in stress-space. In this figure, we consider only the subset of contacts that were fully sliding during the loading phase of isochoric probes in multiple directions (i.e., for  $d\varepsilon_{ij}$  angles  $\theta$  of  $0^\circ$  to  $360^\circ$ ). The top line give the numbers of sliding contacts during loading (i.e., during the segment AB in Fig. 3), normalized by dividing by the number of particles. This subset of contacts can transition to three different conditions during the unloading phase (when  $d\sigma_{ij} \rightarrow -d\sigma_{ij}$ , as in segment BA' in Fig. 3): to an elastic condition, to micro-slip, or to continued sliding (recall the "slip" row in Fig. 4c). Some fraction of contacts slide during loading, regardless of the loading direction  $d\varepsilon_{ij}$ . Moreover, some of the contacts that were sliding during loading continue to slide during unloading. For example, when the loading increment was in the direction triaxial compression ( $\theta = 0^\circ$ ),  $0.56$  contacts per particle were slipping. During the subsequent unloading increment,  $0.56 - 0.42 = 0.14$  continued to slip;  $0.42 - 0.06 = 0.36$  transitioned to micro-slip; and  $0.06$  contacts per particle had transitioned to an elastic condition.

In Fig. 7, we show the vigor of contact sliding for a single isochoric loading–unloading probe: a probe in the direction  $\theta = 90^\circ$  of  $d\varepsilon_{ij}$ , which corresponds to deviatoric loading that is transverse to the original triaxial compression (refer to the " $\odot$ " points in Fig. 6a). The figure represents those contacts that were sliding during both loading and unloading phases of the probe (refer to the "slip→slip" line in Fig. 6c), and each dot represents a single contact among the 1980 contacts that were sliding during both loading and unloading (about 4530 contacts were sliding during loading, but sliding had ceased at all but the 1980 contacts during the unloading phase). The vigor of sliding is given as the rate of frictional dissipation at each contact, with a contact's work rate normalized by dividing by  $p$ , by the cubed mean particle size, and by the bulk strain rate. Although fewer contacts are sliding during unloading, sliding remains vigorous during unloading, and among many contacts, frictional dissipation was *greater* during unloading than during loading. These micro-scale movements are consistent with the results in Fig. 5, in which the directions of contact movement during loading and retrogression (strain reversal) are only weakly counter-correlated, and many contacts continue to move and slip in the same direction during both loading and its reversal.

Figure 8 shows the results of deviatoric, pi-plane isobaric (constant- $p$ ) probes of *equal stress magnitude*,  $|d\sigma_{ij}| = 1$  Pa for the assembly with Cattaneo–Mindlin contacts. Each probe



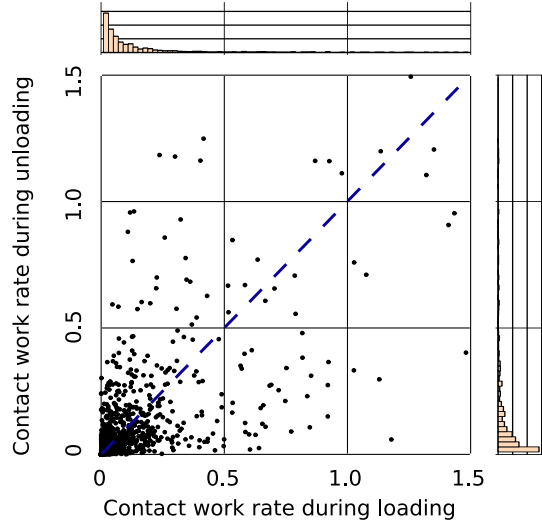


Figure 7: Comparison of sliding rates (work rates) among contacts during the loading and unloading phases of a single isochoric probe with  $\theta = 90^\circ$ . The probe was performed at strain  $\varepsilon = -0.3\%$  with Cattaneo–Mindlin contacts.

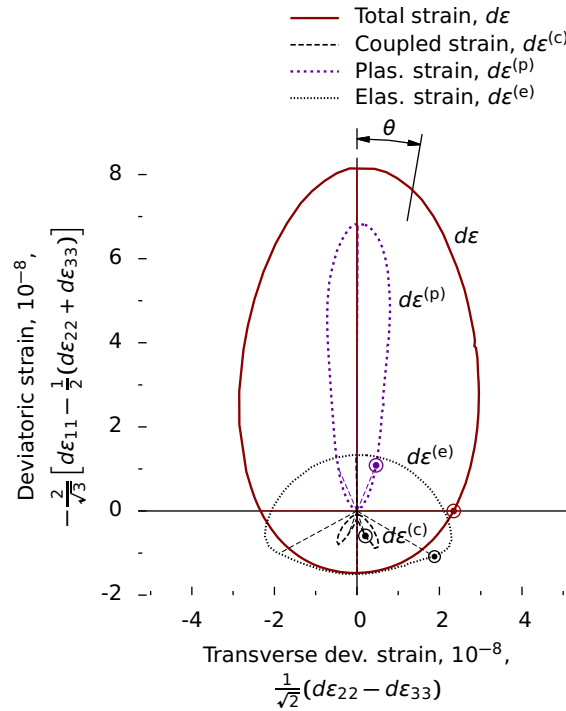


Figure 8: Isobaric probes of magnitude  $|d\sigma_{ij}| = 1$  Pa: total, elastic, plastic, and coupled parts of strain increments for an assembly with Cattaneo–Mindlin contacts at strain  $\varepsilon = -0.3\%$ . Dots “ $\odot$ ” are for a total increment  $d\varepsilon_{ij}$  of transverse deviatoric loading ( $\theta = 90^\circ$ ), and the inset at the top of Fig. 6a shows the addition of the  $d\varepsilon_{ij}^{(e)}$  and  $d\varepsilon_{ij}^{(p)}$  vectors.

had a strain magnitude of  $2 \times 10^{-6}$ , and after noting the resulting stress increment, the strains were scaled to a stress magnitude of 1 Pa. The loci of total, elastic, plastic, and coupled strain increments are displayed as “response envelopes,” in the manner of Gudehus [22]. The effect of elastic-plastic coupling is clear: contrary to conventional models, the elastic strain increment is not of a linear form  $C_{ijkl} d\sigma_{kl}$  (note the *sum* of the first two terms on the right of Eq. 11), as the envelope of elastic increments  $d\varepsilon_{ij}^{(e)}$  is an odd shape and is certainly not an ellipse that would fit the linear form. This result is cautionary: the recoverable (elastic) strain increment is not a linear function of the stress increment, as in a generalized Hooke’s law. One must recall that the elastic moduli are altered by irreversible processes (second term on the right of Eq. 11), as particle rearrangements and frictional contact dissipation in the form of slip and micro-slip accompany plastic deformation. On the other hand, in a separate analysis of the *reversible* strains, we found that the reversible strain increments, indeed, conform closely to a linear form  $C_{ijkl} d\sigma_{kl}$ . (see [34]).

Note also that the plastic envelope is not a straight line emanating from the origin in a single flow direction. That is, plastic strains are not of the form  $g_{ij} f_{kl} d\sigma_{kl}$  for some yield direction  $f_{kl}$  and flow direction  $g_{ij}$ . This aspect of the incremental behavior was noted in the simulations of Kishino [31] and Wan and Pinheiro [49], is quantified by the authors in [34], and is addressed by certain constitutive models with incremental non-linearity [15, 17, 14]. Finally, we note that the locus of plastic increments  $d\varepsilon_{ij}^{(p)}$  does not pass through the origin, as the locus of plastic increments  $d\varepsilon_{ij}^{(p)}$  envelops the origin, and some plastic deformation occurs with all loading directions (as with vanishing elastic range plasticity models [11]).

A separate series of over fifty probes was conducted with different combinations of deviatoric and volumetric strain increments under axisymmetric triaxial conditions. The results in Fig. 9 are presented in the Rendulic plane: the horizontal axis is the volumetric direction (with compression to the right), and the vertical axis is deviatoric strain, as with the vertical axes in Figs. 6a and 8 (upward represents continued axial compression). As with the earlier figures, the probes in Fig. 9 are of magnitude  $|d\varepsilon_{ij}| = 2 \times 10^{-6}$  and were begun during strain hardening, when the stress had reached 55% of peak strength ( $\varepsilon_{11} = -0.3\%$ , Fig. 2). As an example, the dots “ $\odot$ ” show the various incremental parts for a total isotropic increment of volume expansion. The coupled increments are seen to occur primarily in the negative deviatoric direction (i.e. triaxial extension) and can be fairly large when compared with the total strain increment. The locus of irreversible parts is a nearly vertical line, indicating the flow is almost exclusively deviatoric (the initial probe strain of 0.3% is near the transition between contractive and dilatant behaviors). A comparison of the reversible and elastic increments in Figs. 9a and 9b reveals a sharp, non-smooth shape of the elastic response, a consequence of adding the spiked locus of coupled increments to the smooth locus of reversible increments. As was noted with behavior in the pi-plane, the coupled strain part is smallest when the total strain increment is in the direction of continued triaxial compression, but for other directions, the coupled part can be as large as 30% of the total increment. The coupled part is largest during volumetric expansion and is primarily deviatoric.

The simulation results in this section are for the assembly with Cattaneo–Mindlin contacts at the initial probes state of strain  $\varepsilon_{11} = -0.3\%$ . We conducted similar simulations with the assembly having linear–frictional contacts, and the results were qualitatively similar in every respect. Results at other strains are reviewed in the next section.

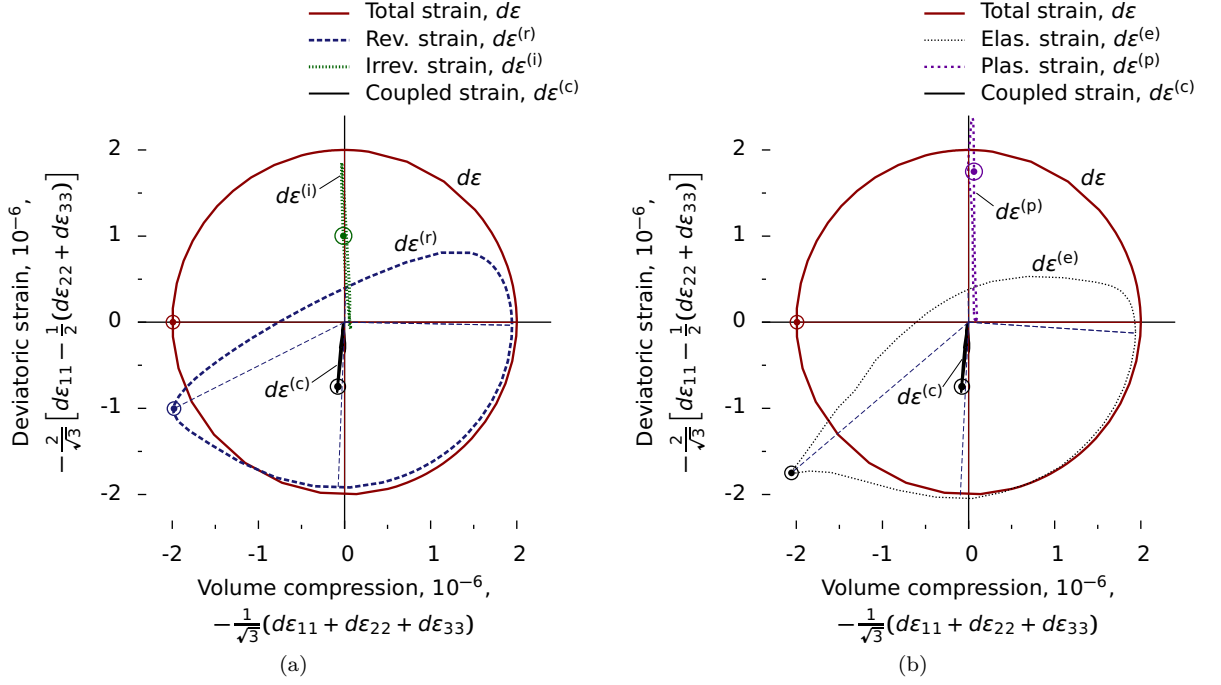


Figure 9: Probes within the triaxial Rendulic plane for the assembly with Cattaneo–Mindlin contacts at strain  $\epsilon = -0.3\%$ : (a) reversible and irreversible parts of the total strain increment; and (b) elastic and plastic parts of the total strain increment. Dots "o" are for a total strain increment of isotropic, volumetric expansion.

## 5. Evolution of reversible and irreversible increments

We now consider the evolution of the reversible, irreversible, and coupled parts of a strain increment, from the start of triaxial loading until a compressive strain of 1% and larger. We conducted Types 2 and 3 stress probes, similar to those described above, at several stages of the constant- $p$  triaxial compression (as in Fig. 2, with axial strain  $\epsilon_{11}$  at constant mean stress  $p$ ). Figures 10a and 10b show the reversible–irreversible and elastic–plastic partitions of the axial and volumetric strain increments for the assembly with Cattaneo–Mindlin contacts, in which probes of the total strain  $d\epsilon_{ij}$  were conducted in the direction of continued axisymmetric constant- $p$  triaxial compression (direction  $\theta = 0^\circ$  in Fig. 6a). Figure 10c shows these partitions for probes conducted in the transverse-deviatoric direction (direction  $\theta = 90^\circ$  in Fig. 6a). Here,  $d\epsilon_2$  represents the transverse deviatoric strain increment  $(d\epsilon_{22} - d\epsilon_{33})/\sqrt{2}$ , which is measured along the horizontal axis in Figs. 6 and 8. The various incremental parts are normalized by dividing by the full increments, either  $d\epsilon_{11}$  or  $d\epsilon_2$ . In Figs. 10a and 10c, the strain partitions are shown in an additive manner; whereas, for the volume increments of Fig. 10b, the four parts (elastic, plastic, reversible, and irreversible) are shown separately.

In regard to deviatoric probes in direction  $\theta = 0^\circ$ , the behavior was almost entirely reversible (and elastic) at the start of loading, with irreversible increments that were nearly zero. Irreversible (and plastic) strain increments increased with increasing axial deformation and dominated the loading behavior at cumulative strains greater than 0.1%. Volume change

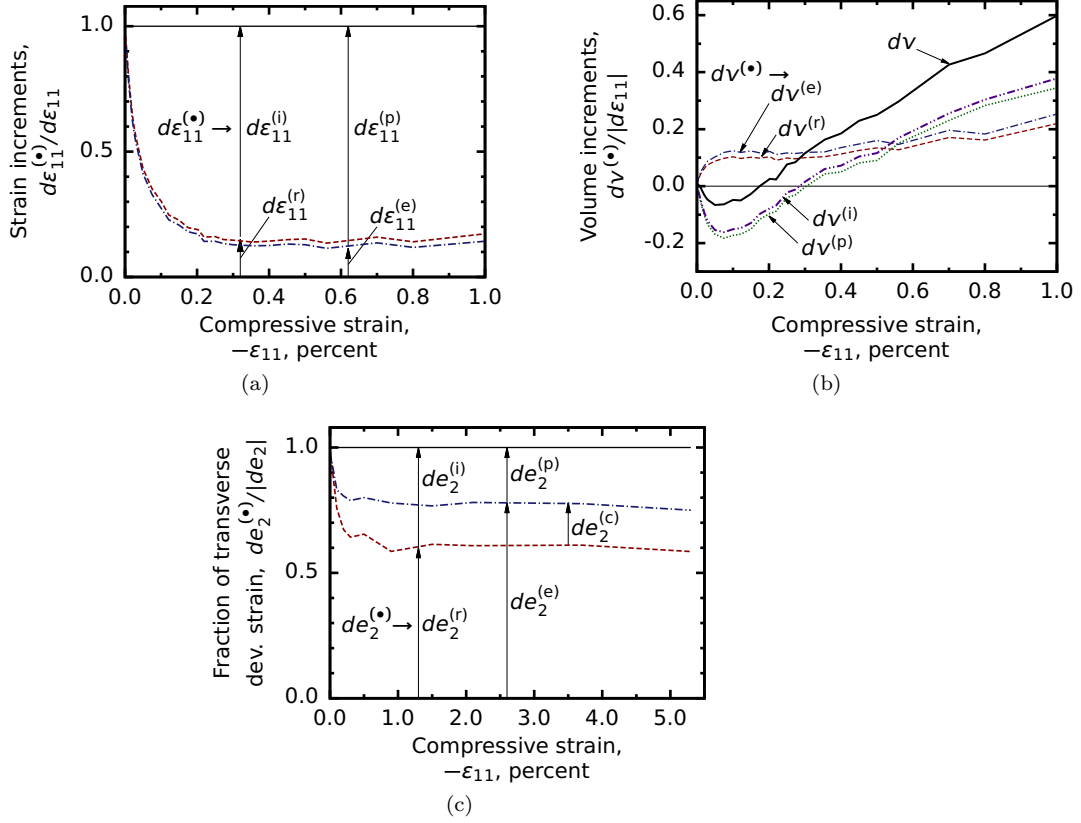


Figure 10: Reversible–irreversible and elastic–plastic partitions of strains during constant- $p$  triaxial compression of the assembly with Cattaneo–Mindlin contacts: (a) axial increments  $d\varepsilon_{11}$  for probes in direction  $\theta = 0^\circ$  (see Fig. 6a); (b) volumetric increments  $dv$  for strains in direction  $\theta = 0^\circ$ ; and (c) transverse-deviatoric strain in direction  $\theta = 90^\circ$ . Strain increments are normalized by dividing by the increments  $d\varepsilon_{11}$  and  $de_2$ . The superscript  $(\bullet)$  in the axes labels can mean (e), (p), (i), (r), or (c).

was contractive at the start of loading and transitioned to dilative behavior at strain 0.2% (Fig. 10b, note that the transition for plastic strains occurred at a strain of about 0.3%). Throughout the constant- $p$  loading (i.e. axial loading while maintaining constant mean stress), the reversible (and elastic) deformation was dilative with a rate  $dv^{(r)}/|d\varepsilon_{11}|$  between 0 and 0.23. The particle arrangement was initially isotropic, and at zero strain, the elastic response exhibited no volume change during the constant- $p$  loading. Upon further loading, however, the fabric became increasingly anisotropic, as the material became elastically stiffer in the axial  $d\varepsilon_{11}$  direction (elastic hardening), while becoming softer in the transverse directions (elastic softening). At a strain of 0.5%, the reversible Young’s modulus in the axial direction was more than twice the transverse modulus, giving rise to the reversible dilation, for constant- $p$  loading, seen in Fig. 10b (see [34] for further analysis of the reversible moduli). The irreversible (and plastic) volume rate transitioned from contractive, at the start of loading, to dilative, at strains greater than 0.2% and was responsible for the initial contractive behavior. Throughout loading, a coupled “c” part was present, although small,

for the probes in direction  $\theta = 0^\circ$  of continued triaxial loading, and the coupled part appears as the thin difference between the elastic (“e”) and recoverable (“r”) lines.

Although it is small for probes of continued triaxial compression, Fig. 10c shows that the coupled part was significant for transverse-deviatoric probes in direction  $\theta = 90^\circ$  (see Figs. 6 and 8 and the “ $\odot$ ” symbols that correspond to the  $\theta = 90^\circ$  direction). The coupled part of the strain increment,  $de_2^{(c)}$ , is significant for this probe direction and accounts for 15–20% of the total transverse strain for axial strains greater than 0.2%.

## 6. Conclusions

Bulk deformation of a granular material produces contact frictional dissipation in the form of slip and micro-slip at the inter-particle contacts. The aggregate effect of this contact-scale dissipation is stress-work expended in plastic deformation and in irreversible alterations of the particle arrangements and contact conditions. When a strain increment is reversed,  $d\epsilon \rightarrow -d\epsilon$ , or when a stress increment is reversed,  $d\sigma \rightarrow -d\sigma$ , the contact movements are not necessarily reversed, and some contacts that were undergoing slip or micro-slip during a forward increment continue to slip during the reversed retrogression or unloading increment. That is, frictional contact dissipation and irreversible deformation occur during both forward and reversed increments, and if a strictly elastic region of loading exists at all, it is smaller than the strain increments of  $2 \times 10^{-6}$  that were used in our simulations. In the context of thermomechanics, granular materials are coupled materials in the sense that increments of elastic strain are altered by changes in the elastic moduli that occur concurrently with the loading increment and are associated with irreversible micro-scale changes within the material. The difference between the conventional elastic (recoverable) strain increment and the reversible part of the increment is a coupling part  $d\epsilon^{(c)}$ . This coupled part is small during conventional triaxial loading conditions and might escape notice in a laboratory setting or even in DEM simulations, but the coupled increments are quite large for other loading directions and produce a significant difference between the elastic–plastic and reversible–irreversible partitions of a total strain increment.

Our measurements of the reversible, irreversible, and coupled parts of strain increments were obtained through rather extraordinary intervention: by suppressing the slip and micro-slip that would otherwise occur at the contacts, as in [6]. This sort of intrusion or internal constraint is not available with laboratory testing, which relies on loading–unloading cycles to determine the elastic and plastic parts of strain. Even though our simulation methods can not be replicated in physical tests, the implications of our simulation are certainly cautionary: elastic strain increments are accompanied by micro-scale irreversible processes that alter the elastic moduli during plastic deformation, and the application of elastic strains in constitutive formulations should be done with this understanding. For example, the shape of the response envelopes of elastic increments in Fig. 8 indicates the difficulty of applying a linear Hooke stiffness to the *elastic* strain increments, although in a related work we show that a linear stiffness relation precisely fits the *reversible* increments [34].

All of the forgoing conclusions apply to simulations with either of two contact models: with the simple linear-frictional model and with the more complex Hertz-type Cattaneo–Mindlin model. Although we have described behavior that is complex and inconsistent with simple constitutive models, the simulations do show that the bulk large-strain behavior of granular materials during monotonic loading is somewhat insensitive to the details of the contact model, provided that the simulations include a common friction coefficient.

Our study was limited to behavior that followed an initial monotonic drained triaxial compression, and this work could certainly be extended to more general loading paths: other proportional loading paths, paths involving principal stress rotations, and cyclic paths. The results suggest, however, that granular behavior is even more complex than previously thought and that granular materials should be treated as coupled and thoroughly inelastic.

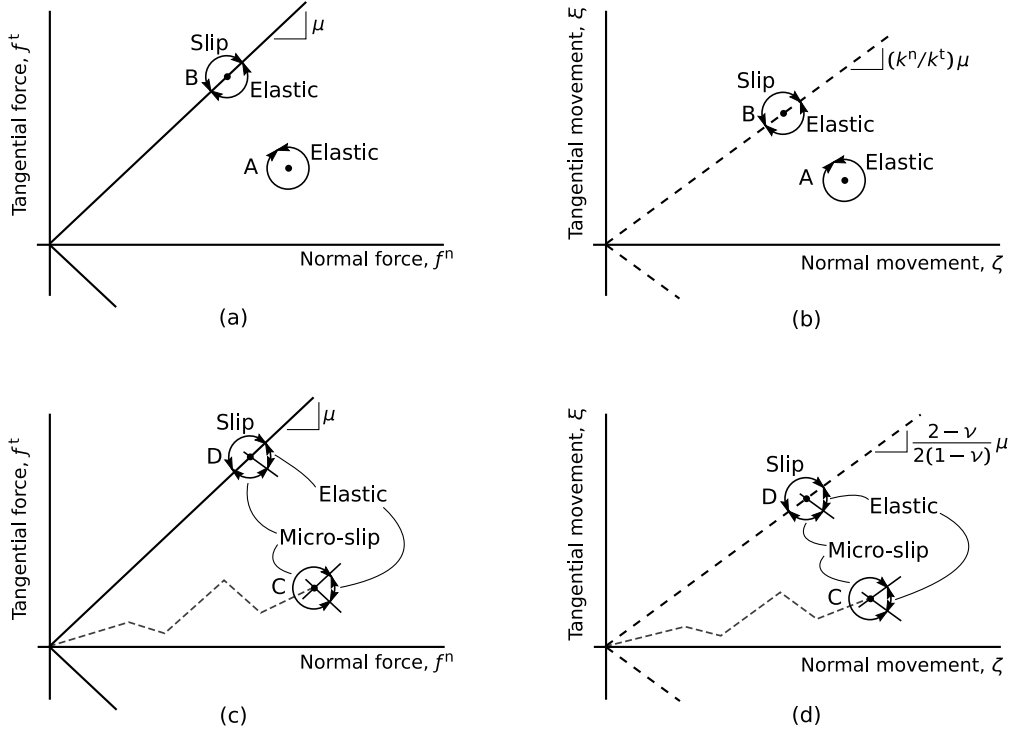


Figure A.11: Contact yield surfaces in force-space and movement-space for two contact models: (a) force-space for linear-frictional contacts; (b) displacement-space for linear-frictional contacts; (c) force-space for Cattaneo–Mindlin contacts; and (d) displacement-space for Cattaneo–Mindlin contacts.

## Appendix A. Incremental behavior of contact models

Figure A.11 depicts the two contact models — linear-frictional and Cattaneo–Mindlin — that were used in the simulations. Figures A.11a and A.11b are of the simpler linear-frictional model, showing the two-dimensional spaces of forces and movements, with  $f^n$  and  $\zeta$  representing the normal components of compressive contact force and displacement, and  $f^t$  and  $\xi$  representing the tangential displacement and force. (In a three-dimensional setting,  $\mathbf{f}^t$  and  $\boldsymbol{\xi}$  are vectors that lie in the contact’s tangent plane.) The behavior of the linear-frictional model is entirely reversible for points within the contact yield cone having its apex at the  $f^n$ – $f^t$  origin (e.g., the behavior is reversible at points “A” in Figs. A.11a and A.11b). When the frictional limit is reached (points “B”) and  $|\mathbf{f}^t| = \mu f^n$ , slip can commence and the zone of incremental reversibility is a semi-space inside of the yield cone. In the force-space of Fig. A.11a, the reversible and irreversible (“slip”) conditions are represented by small arced arrows (actually, filled cones in 3-space) that show the corresponding ranges of the force increments. In the strain-space of Fig. A.11b, reversible and irreversible (slip) increments are shown in a similar manner, but the orientation of the yield boundary (cone) has slope  $\mu k^n/k^t$ , where  $k^n$  and  $k^t$  are the linear contact stiffnesses in the normal and tangential directions. The increment of frictional energy dissipation during a small tangential movement  $\Delta \xi$  is computed as the incremental difference of the work done by the tangential force,  $\mathbf{f}^t \cdot \Delta \boldsymbol{\xi}$ , and

the change of elastic energy of the contact,  $\Delta[(\mathbf{f}^t)^2/2k^n]$ .

The simple linear-frictional contact yields a small-strain bulk shear modulus that is independent of the mean stress — a condition that poorly represents the behavior of most geomaterials. For this reason, a generalized Cattaneo–Mindlin contact is considered a better representation of the particle interactions [35].

The incremental force-displacement relation of the Cattaneo–Mindlin contact is quite complex and depends on the history of both normal and tangential movements. Mindlin and Deresiewicz [39] derived the contact stiffnesses for eleven such histories of contact movement, and Jäger [29] developed a general framework for the Cattaneo–Mindlin contact that encompasses arbitrary sequences of contact movement. The “Jäger contact” is incorporated in the authors’ OVAL code (see [33, 35]). Because contact behavior is history-dependent, a contact’s history is recorded as an “equivalent load history”, represented by the dashed lines in Figs. A.11c and Figs. A.11d: a piece-wise linear sequence of displacement pairs  $\zeta^*$  and  $\xi^*$  (or, in force-space, pairs  $f^{*t}$  and  $f^{*n}$ ). The full list of these pairs comprise the internal condition (the “internal variables”) of this single contact. For forces that lie *inside* the cone of full frictional slip (points “C”, Fig. A.11), the incremental reversible domain is quite restricted. Reversible contact displacement is limited to the following: (1) increments that lie inside the cone of slope  $\mu\kappa$  in displacement-space ( $\mu$  in force-space) and (2) paths of perfect reversal that “back track” along the equivalent load history (factor  $\kappa = (2 - \nu)/2(1 - \nu)$ ,  $\nu$  being the Poisson ratio  $\nu$  of the grains [29, 33]). Dissipative annular micro-slip occurs for all other increments. When the frictional limit is reached (i.e.,  $|\mathbf{f}^t| = \mu f^n$ , as at points “D”), the incremental contact behavior can be one of three types: reversible, micro-slip (reversible-irreversible), or slip (irreversible), depending on the loading direction. Compared with the linear-frictional model of Figs. A.11a and A.11b, a Hertz-like Cattaneo–Mindlin contact is more complex and has smaller reversible zones (cones), and this contact behavior is expected to produce a smaller, more restricted reversible region for the bulk material behavior than that of the simpler linear-frictional model.

The computation of frictional contact dissipation is also straightforward with a Cattaneo–Mindlin contact, provided that the contact is in full frictional slip (points “D” in Fig. A.11). Computing dissipation is more difficult in the case of micro-slip for Cattaneo–Mindlin contacts that have not yet reached the frictional limit (points “C” in Fig. A.11). For each time increment  $\Delta t$  in our DEM simulations with Cattaneo–Mindlin contacts, we computed the increment of reversible tangential displacement  $\Delta\xi^{(r)}$ , subtracted this reversible increment from the full increment  $\Delta\xi$  to find the irreversible tangential increment,

$$\Delta\xi^{(i)} = \Delta\xi - \Delta\xi^{(r)} \quad (\text{A.1})$$

and then computed the inner produce of the irreversible increment and the tangential force to find the increment of dissipation:

$$\text{Contact dissipation} = \mathbf{f}^t \cdot \Delta\xi^{(i)} \quad (\text{A.2})$$

To find the incremental reversible tangential movement  $\Delta\xi^{(r)}$  in Eq. (A.1), which represents the response to the increment of tangential force  $\Delta\mathbf{f}^t$  *in the absence of micro-slip*, we used Walton’s solution for the tangential contact response of rough (zero-slip) spheres [48]:

$$\Delta\xi^{(r)} = \frac{2 - \nu}{8G} \frac{1}{a} \Delta\mathbf{f}^t \quad (\text{A.3})$$



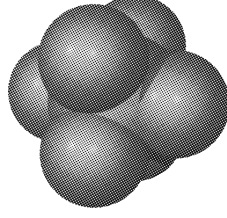


Figure B.12: Sphere-cluster particle.

where  $G$  is the particle's shear modulus,  $\nu$  is its Poisson ratio, and  $a$  is the current radius of the contact zone. For sphere–sphere contact,  $a$  is the geometric mean of the contact indentation and sphere radius ( $a = \sqrt{\zeta R}$ ); for non-spherical asperities of the power-law type ( $z = A_\alpha r^\alpha$ ), Jäger [28] derived the radius as

$$a = \left[ \frac{\zeta}{\alpha \sqrt{\pi}} \frac{\Gamma(\frac{\alpha+1}{2})}{\Gamma(\frac{\alpha+2}{2})} \right]^{1/\alpha} \quad (\text{A.4})$$

where  $\Gamma(\cdot)$  is the gamma function.

In this manner, we tracked the frictional dissipation of each Cattaneo–Mindlin contact so that the total contact frictional dissipation and total contact elastic energy of the assemblies could be computed. Note that the elastic (reversible) movement  $\Delta \xi^{(t)}$  depends upon the contact radius  $a$  and hence upon the indentation  $\zeta$  and normal force  $f^n$ .

## Appendix B. DEM modeling details and quasi-static verification

Discrete element simulations were conducted with a cubical assembly of 10,648 particles contained within periodic boundaries. The simulations were intended to produce a modest fidelity to the bulk behavior of sands at low confining stress. Because sphere assemblies produce unrealistic rolling between particles and have a low bulk strength, we used a bumpy, non-convex cluster shape for the particles: a large central sphere with six smaller embedded outer spheres in an octahedral arrangement (Fig. B.12). The use of non-spherical particles circumvents the need of artificial measures to restrain the particle rotation (for example, the use of rotational contact springs or the direct restraint of particle rotations, as in [6, 43]). Through trial and error, we chose the radii of the central and outer spheres so that the bulk behavior approximated that of Nevada Sand, a standard poorly graded sand (SP) use in laboratory and centrifuge testing programs [4, 35]. The particle size range was 0.074–0.28 mm, with  $D_{50} = 0.165$  mm.

To create assemblies with a range of densities, we began with the particles sparsely and randomly arranged within a cubic periodic cell. With an initial low inter-particle friction coefficient ( $\mu = 0.20$ ), the assembly was isotropically reduced in dimension until it “seized” when a sufficiently complete contact network had formed. A series of 25 progressively denser assemblies were created by repeatedly assigning random velocities to the particles of the previous assembly and then further reducing the cell's dimensions until it, too, had seized. The 25 assemblies had void ratios ranging from 0.781 to 0.586 (solid fractions of 0.561 to 0.664). The single assembly used in the paper had void ratio 0.690 (solid fraction 0.592) and

approximates the behavior of Nevada Sand at a relative density of 40%. After compaction, the assembly was allowed to quiesce with friction coefficient  $\mu = 0.40$ , which was then raised to  $\mu = 0.55$  for the subsequent loading simulations.

The particles are durable (non-breaking) and interact only at their contacts. Two contact models were used in the simulations: linear springs with friction, and a Hertz, Cattaneo–Mindlin model, as described in Section 1.3 and Appendix A. The Cattaneo–Mindlin model was a full implementation of a Hertz–Mindlin contact between elastic-frictional bodies. We used the Jäger algorithm, which can model arbitrary sequences of normal and tangential contact movements [33]. With the Cattaneo–Mindlin contacts, the loading simulations were conducted with an inter-particle friction coefficient  $\mu = 0.55$ , particle shear modulus  $G = 29$  GPa, and Poisson ratio  $\nu = 0.15$ .

As has been noted by Alonso-Marroquín et al. [2] and Froiio and Roux [19], DEM simulations necessarily involve a compromise between scientific intent and computational expedience. Without proper care, DEM simulations can yield results that are sensitive to strain rate, due to the particles’ inertias and to the damping that is employed to stabilize the particles’ motions [46]. Our intent was to model behavior in which these effects were minimized so that rate-independent behavior was attained. To this end, we used a slow strain rate (strain increments of  $1 \times 10^{-8}$ ) and minimal viscous damping (2% of critical damping).

Several performance parameters were used to verify the quasi-static and rate-independent nature of these probes. The inertial number  $I = \dot{\epsilon} \sqrt{m/(pd)}$ , a relative measure of loading and inertial rates, was about  $1 \times 10^{-11}$ , signifying nearly quasi-static loading [10]. During the incremental probes, the average imbalance of force on a particle was less than 0.003% of the average contact force (parameter  $\chi$  in [42, 46]). The average kinetic energy of the particles was less than  $3 \times 10^{-7}$  times the elastic energy in the contacts. With the very slow strain rates of the simulations, doubling the strain increment from  $1 \times 10^{-8}$  to  $2 \times 10^{-8}$  had minimal effect on the monotonic stress-strain response. Boundary movements were regulated so that any six of the stress or strain components (or any six linear combination of these components) could be controlled at desired rates. When a stress component was controlled, it would typically remain on target to within 0.001 Pa, compared with the mean stress of 100 kPa and stress-probes that produced stress changes  $|d\sigma_{ij}|$  on the order of 100 Pa. As further verification of strain rate indifference during loading, we also conducted brief creep and stress relaxation tests in which either the stress or the assembly boundaries were frozen at the end of a stress probe. Froiio and Roux [19] have noted a tendency for an assembly to exhibit creep during small stress probes, an inclination that can obscure the probe results. During our creep tests, the strain rate was  $0.5\text{--}3 \times 10^{-10}$ , far less than the loading rate of  $1 \times 10^{-8}$ . During stress relaxation with zero strain rate, the stress changed at a rate of less than 4% of that typically measured during the incremental stress probes that were used in this study. The strain increment of  $2 \times 10^{-6}$  and strain steps of  $1 \times 10^{-8}$  entailed 200 steps. Although small fluctuations were noted in the first few steps, the advance of stress and strain were fairly uniform within the 200 strain steps. Moreover, the envelopes in Figs. 6, 8, and 9 are quite smooth, even near the origin of these plots, where the strain parts are minuscule, and at high magnification, indicating that random errors are negligible. All of these measurements indicate that the behavior in the simulations was nearly quasi-static and independent of loading rate.

## References

- [1] F. Alonso-Marroquín, H. Herrmann, The incremental response of soils. an investigation using the discrete-element method, *J. Eng. Math.* 52 (1-3) (2005) 11–34.
- [2] F. Alonso-Marroquín, S. Luding, H. J. Herrmann, I. Vardoulakis, Role of anisotropy in the elastoplastic response of a polygonal packing, *Phys. Rev. E* 71 (5) (2005) 051304.
- [3] A. Anandarajah, K. Sobhan, N. Kuganenthira, Incremental stress-strain behavior of granular soil, *J. Geotech. Eng.* 121 (1) (1995) 57–68.
- [4] K. Arulmoli, K. K. Muraleetharan, M. M. Hossain, L. S. Fruth, VELACS verification of liquefaction analyses by centrifuge studies laboratory testing program soil data report, Tech. Rep. Project No. 90-0562, The Earth Technology Corporation, Irvine, CA, data available through <http://yees.usc.edu/velacs> (1992).
- [5] J. P. Bardet, Observations on the effects of particle rotations on the failure of idealized granular materials, *Mech. of Mater.* 18 (2) (1994) 159–182.
- [6] F. Calvetti, G. Viggiani, C. Tamagnini, A numerical investigation of the incremental behavior of granular soils, *Rivista Italiana di Geotecnica* 3 (2003) 11–29.
- [7] B. D. Coleman, M. E. Gurtin, Thermodynamics with internal state variables, *J. Chem. Phys.* 47 (2) (1967) 597–613.
- [8] I. F. Collins, G. T. Houlsby, Application of thermomechanical principles to the modelling of geotechnical materials, *Proc. R. Soc. Lond. A* 453 (1964) (1997) 1975–2001.
- [9] P. A. Cundall, Computer simulations of dense sphere assemblies, in: M. Satake, J. Jenkins (eds.), *Micromechanics of Granular Materials*, Elsevier Science Pub. B.V., Amsterdam, The Netherlands, 1988, pp. 113–123.
- [10] F. da Cruz, S. Emam, M. Prochnow, J.-N. Roux, F. Chevoir, Rheophysics of dense granular materials: Discrete simulation of plane shear flows, *Phys. Rev. E* 72 (2) (2005) 021309.
- [11] Y. Dafalias, On cyclic and anisotropic plasticity, Ph.D. thesis, University of California, Berkeley, California, USA (1975).
- [12] Y. F. Dafalias, Elasto-plastic coupling within a thermodynamic strain space formulation of plasticity, *Int. J. Non-linear Mech.* 12 (5) (1977) 327–337.
- [13] Y. F. Dafalias, Il'iusin's postulate and resulting thermodynamic conditions on elasto-plastic coupling, *Int. J. Solids Struct.* 13 (3) (1977) 239–251.
- [14] Y. F. Dafalias, M. Taiebat, SANISAND-Z: zero elastic range sand plasticity model, *Géotechnique* 66 (12) (2016) 999–1013.
- [15] F. Darve, Contribution a la determination de la loi rheologique incrementale des sols, These de docteur-ingénieur, Univ. Sci. et Medicale de Grenoble, France (1974).
- [16] F. Darve, The expression of rheological laws in incremental form and the main classes of constitutive equations, in: F. Darve (ed.), *Geomaterials: constitutive equations and modelling*, Elsevier, London, 1990, pp. 123–147.
- [17] F. Darve, S. Labanieh, Incremental constitutive law for sands and clays: simulations of monotonic and cyclic tests, *Int. J. Numer. and Anal. Methods in Geomech.* 6 (2) (1982) 243–275.
- [18] D. Elata, J. G. Berryman, Contact force-displacement laws and the mechanical behavior of random packs of identical spheres, *Mech. of Mater.* 24 (3) (1996) 229–240.
- [19] F. Froio, J.-N. Roux, Incremental response of a model granular material by stress probing with dem simulations, in: J. Goddard, P. Giovine, J. T. Jenkins (eds.), *IUTAM-ISIMM Symposium on mathematical modeling and physical instances of granular flow*. AIP Conference Proceedings, vol. 1227, AIP, 2010, pp. 183–197.
- [20] A. Gajo, The influence of system compliance on collapse of triaxial sand samples, *Can. Geotech. J.* 41 (2) (2004) 257–273.
- [21] M. Gonzalez, A. M. Cuitiño, A nonlocal contact formulation for confined granular systems, *J. Mech. Phys. Solids* 60 (2) (2012) 333–350.
- [22] G. Gudehus, D. Kolymbas, A constitutive law of rate type for soils, in: W. Wittke (ed.), *Numerical Methods in Geomechanics Aachen 1979*, vol. 1, A. A. Balkema, Rotterdam, 1979, pp. 319–329.
- [23] B. Harthong, J.-F. Jérier, V. Richefeu, B. Chareyre, P. Dorémus, D. Imbault, E.-V. Donzé, Contact impingement in packings of elastic-plastic spheres, application to powder compaction, *Int. J. of Mech. Sci.* 61 (1) (2012) 32–43.
- [24] R. Hill, The essential structure of constitutive laws for metal composites and polycrystals, *J. Mech. Phys. Solids* 15 (2) (1967) 79–95.
- [25] T. Hueckel, Coupling of elastic and plastic deformations of bulk solids, *Meccanica* 11 (4) (1976) 227–235.
- [26] T. Hueckel, G. Maier, Incremental boundary value problems in the presence of coupling of elastic and plastic deformations: a rock mechanics oriented theory, *Int. J. Solids Struct.* 13 (1) (1977) 1–15.
- [27] T. Hueckel, R. Nova, Some hysteresis effects of the behaviour of geologic media, *Int. J. Solids Struct.* 15 (8) (1979) 625–642.
- [28] J. Jäger, Uniaxial deformation of a random packing of particles, *Arch. Appl. Mech.* 69 (3) (1999) 181–203.
- [29] J. Jäger, *New Solutions in Contact Mechanics*, WIT Press, Southampton, UK, 2005.

- [30] J. Kestin, J. R. Rice, Paradoxes in the application of thermodynamics to strain solids, in: E. B. Stuart, G.-O. B., A. J. Brainard (eds.), *A Critical Review of Thermodynamics*, Mono Book Corp., Baltimore, 1970, pp. 275–298.
- [31] Y. Kishino, On the incremental nonlinearity observed in a numerical model for granular media, *Revista Italiana Di Geotecnica* 3 (2003) 30–38.
- [32] M. R. Kuhn, OVAL and OVALPLOT: programs for analyzing dense particle assemblies with the Discrete Element Method, <http://faculty.up.edu/kuhn/oval/oval.html>.
- [33] M. R. Kuhn, Implementation of the Jäger contact model for discrete element simulations, *Int. J. Numer. Methods Eng.* 88 (1) (2011) 66–82.
- [34] M. R. Kuhn, A. Daouadji, Multi-directional behavior of granular materials and its relation to incremental elastoplasticity, In review.
- [35] M. R. Kuhn, H. Renken, A. Mixsell, S. Kramer, Investigation of cyclic liquefaction with discrete element simulations, *J. Geotech. and Geoenv. Eng.* 140 (12) (2014) 04014075.
- [36] A. Lashkari, A. Golchin, On the influence of elastic–plastic coupling on sands response, *Comput. and Geotech.* 55 (2014) 352–364.
- [37] X. Lin, T.-T. Ng, A three-dimensional discrete element model using arrays of ellipsoids, *Géotechnique* 47 (2) (1997) 319–329.
- [38] J. Mandel, Thermodynamics and plasticity, in: J. D. Domingos, M. N. R. Nina, J. H. Whitelaw (eds.), *Foundations of Continuum Thermodynamics*, John Wiley and Sons, New York, 1973, pp. 283–304.
- [39] R. Mindlin, H. Deresiewicz, Elastic spheres in contact under varying oblique forces, *J. Appl. Mech.* 19 (1) (1953) 327–344.
- [40] Z. Mróz, V. A. Norris, O. C. Zienkiewicz, An anisotropic hardening model for soils and its application to cyclic loading, *Int. J. Numer. and Anal. Methods in Geomech.* 2 (3) (1978) 203–221.
- [41] S. Nemat-Nasser, On nonequilibrium thermodynamics of continua, in: S. Nemat-Nasser (ed.), *Mechanics Today: Pergamon Mechanics Today Series*, vol. 2, Pergamon Press Inc., New York, 2013, pp. 94–158.
- [42] T.-T. Ng, Input parameters of discrete element methods, *J. Eng. Mech.* 132 (7) (2006) 723–729.
- [43] J.-P. Plassiard, N. Belheine, F.-V. Donzé, A spherical discrete element model: calibration procedure and incremental response, *Granul. Matter* 11 (5) (2009) 293–306.
- [44] J. R. Rice, Inelastic constitutive relations for solids: An internal-variable theory and its application to metal plasticity, *J. Mech. Phys. Solids* 19 (6) (1971) 433–455.
- [45] P. Royis, T. Doanh, Theoretical analysis of strain response envelopes using incrementally non-linear constitutive equations, *Int. J. Numer. and Anal. Methods in Geomech.* 22 (2) (1998) 97–132.
- [46] K. Suzuki, M. R. Kuhn, Uniqueness of discrete element simulations in monotonic biaxial shear tests, *Int. J. Geomech.* 14 (5) (2014) 06014010.
- [47] C. Tamagnini, F. Calvetti, G. Viggiani, An assessment of plasticity theories for modeling the incrementally nonlinear behavior of granular soils, *Journal of engineering mathematics* 52 (1-3) (2005) 265–291.
- [48] K. Walton, The oblique compression of two elastic spheres, *J. Mech. Phys. Solids* 26 (3) (1978) 139–150.
- [49] R. Wan, M. Pinheiro, On the validity of the flow rule postulate for geomaterials, *Int. J. Numer. and Anal. Methods in Geomech.* 38 (8) (2014) 863–880.
- [50] H. Ziegler, *An Introduction to Thermomechanics*, North-Holland Pub. Co., Amsterdam, 1983.